Exploring the microstructure, mechanical properties, and corrosion resistance of innovative bioabsorbable Zn-Mg-(Si) alloys fabricated via powder metallurgy techniques

David Nečas [a], Vojtěch Hybášek [a], Jan Pinc [a,b], Andrea Školáková [b], Ilona Voňavková [a], Klára Hosová [a], Martin Zlámal [c], Anna Boukalová [a], Jan Pokorný [a], Drahomír Dvorský [b], Peter Minárik [d], Josef Veselý [d], Črtomir Donik [e], Dalibor Vojtěch [a], Jiří Kubásek [a,*]

[a] Department of Metals and Corrosion Engineering, Faculty of Chemical Technology, University of Chemistry and Technology Prague, Technická 5, 166 28, Praha 6 – Dejvice, Czech Republic
[b] Department of Functional Materials, Institute of Physics of the Czech Academy of Sciences, Na Slovance 1999/2, 182 21, Prague 8, Czech Republic
[c] Department of Inorganic Technology, Faculty of Chemical Technology, University of Chemistry and Technology Prague, Technická 5, 166 28, Praha 6 – Dejvice, Czech Republic
[d] Charles University, Faculty of Mathematics and Physics, Department of Physics of Materials, Ke Karlovu 5, 121 16, Prague, Czech Republic
[e] Institute of Metals and Technology, Lepi Pot 11, SI-1000, Ljubljana, Slovenia

ARTICLE INFO

ABSTRACT

Zinc alloys belong to the widely studied materials for applications like medical devices, however, they often encounter an inappropriate combination of mechanical/corrosion/biological properties. In this respect, we produced the Zn–1Mg and Zn–1Mg–1Si containing biologically friendly elements with potential strengthening effects on zinc matrix by powder metallurgy methods including mechanical alloying, spark plasma sintering, and extrusion further enabling the formation of materials with unique extremely fine-grained microstructures. The systematic study of these materials showed the possibility of reaching homogeneous nano-grain microstructure and high strength values exceeding 450 MPa in tension. Selected chemical composition and processing methods led also to slightly decreased wear and corrosion rates and rather uniform corrosion.

1. Introduction

Researchers are currently developing new biodegradable metals to address the limitations of traditional implant materials. These new materials aim to mitigate issues such as stress shielding, which can lead to bone degradation and implant loosening, as well as the release of potentially harmful ions such as aluminum, vanadium, chromium, and nickel due to wear or corrosion. The goal is to create materials that support tissue regeneration and dissolve completely after the regenerative process has occurred [1–4]. Additionally, it is important that the by-products of these materials are able to be metabolized by the body without causing any harmful reactions [5]. Despite a variety of materials being studied for these purposes, research has primarily focused on

essential elements such as iron, zinc, magnesium, and their alloys [1–5].

Of the biodegradable metals being studied, zinc has been found to have ideal corrosion resistance compared to magnesium or iron and excellent biocompatibility [5]. However, it has been repeatedly found to have inadequate mechanical properties for medical applications [2]. To address this issue, researchers have been exploring the use of alloying elements such as magnesium [6,7], manganese [8], copper [9,10], lithium [11,12], etc. to improve the mechanical properties of zinc. Alloying elements may cause the strengthening of the solid solution or precipitated intermetallic phases. Additionally, thermomechanical processes such as rolling [13,14], ECAP (equal-channel angular pressing) [15], extrusion [16,17], etc. have been used to improve the mechanical properties of zinc enabling the reduction of grain size and redistribution

of intermediate phases in the microstructure [18].

In the presented study we tended to improve the mechanical properties of zinc by combination of alloying with Mg and Si and processing of materials by powder metallurgy methods. Magnesium was selected as a key alloying element due to its excellent biocompatibility and its overall strengthening effect on the alloy through the precipitation of hard intermetallic phases such as Mg_2Zn_{11} and $MgZn_2$ [19]. However, it was found that the addition of more than 1 wt% of magnesium can lead to a significant decrease in elongation due to the increased amount of brittle intermetallic phases [20] making Zn–1Mg a widely studied and recommended binary alloy [21–23]. Silicon, on the other hand, is a trace element in the human body that positively affects bone calcification and the generation of the intracellular matrix [24,25]. Studies have shown that silicon-doped materials can increase cell surface adhesion and enhance bioactivity, which is thought to be due to the reaction with water inside the human body. This leads to the formation of Si–OH groups that can induce apatite formation [25]. Unlike magnesium, silicon does not form a solid solution with zinc or intermetallic phases, but it may act as a reinforcement within the microstructure, increasing abrasive properties and creep resistance [26]. Besides, when combined with magnesium, silicon generates the Mg_2Si intermetallic phase enabling it to prevent slip at grain boundaries and improving the creep resistance. The use of hard particles as a reinforcement and preparation of zinc composites containing SiC [27], SiC whiskers [28], and ZrO_2 [29] as reinforcements has been studied in the literature with positive results on mechanical properties, grain-refinement, and bioactivity. A comparable approach to enhance the mechanical properties was employed for Mg-based biodegradable glasses by incorporating reinforcements such as SnZn [30] or pure Fe [31,32]. These composite materials, prepared by combination of powder metallurgy processes and spark plasma sintering, exhibit enhancements in both strength and elongation, achieving improvements of tens of percentages compared to the original [30–32].

Both the alloying elements are poorly soluble (Mg) or not soluble (Si) in the zinc. Therefore, mechanical alloying has been selected for materials production allowing to increase the solubility of selected elements in zinc over equilibrium conditions. Such conditions are more favored from the point of homogeneous uniform degradation. Furthermore, extremely fine-grained homogeneous microstructures with various intermediate phases may be formed during this process [33–35]. To preserve such conditions of powder precursors also for compact materials, a fast compaction technique - Spark Plasma Sintering (SPS) [36,37] has been selected with subsequent extrusion enabling to densifying of the material and affecting phase distribution. The effectiveness of these methods has been previously confirmed in studies on Zn–1Mg (wt. %) alloy, where the microstructure contained grains and intermetallic phases with a size of several hundreds of nanometers [38].

2. Materials and methods

2.1. Materials processing

In this study, Zn–1Mg–1Si (wt. %) and Zn–1Mg (wt. %, reference material) were prepared by mechanical alloying using pure zinc powder (99.9 %, particle size <149 μm, Thermo Fisher Scientific), pure magnesium (99.8 %, particle size <44 μm, Alfa Aesar), and pure silicon (99.5 %, particle size <44 μm, Thermo Fisher Scientific) as the input materials. To prevent the agglomeration of powder particles during milling, 0.03 g of stearic acid was added to all selected compositions. For longer milling times (8 h), the process was divided into two segments (4 h + 4 h) with the same amount of stearic acid added in both segments to prevent sticking of the powder to the milling vessel, decreasing the efficiency of the milling process. The powder mixtures were mechanically alloyed under various conditions (Table 1). The weight of the input powder mixture was 30 g. The milling was performed in ZrO_2 vessels under an argon-protective atmosphere (purity 99.95 %) in a Retsch E-Max milling machine with 800 rotations per minute (RPM). The reverse

Table 1
Conditions of mechanical alloying.

Composition	Rotation speed	Time [h]	Diameter of the milling balls [mm]
Zn–1Mg–1Si	800	0.5	10
Zn–1Mg–1Si		1	10
Zn–1Mg–1Si		2	10
Zn–1Mg–1Si		4	10
Zn–1Mg–1Si		8	5
Zn–1Mg–1Si		8	10
Zn–1Mg–1Si		8	15
Zn–1Mg		8	15

rotation mode was selected with changes in rotation direction every 10 min. The mill is equipped with a water-cooling system enabling it to keep the temperature of the process low (the temperature of the cooling medium was maintained between 30 and 50 °C). The milling balls were composed of ZrO_2 while the ball-to-powder weight ratio was equal to 5:1.

In the mechanical alloying process, the size of the milling balls can impact the amount of energy generated inside the vessels during their collision. This energy can be calculated for E-max mills using equations that consider parameters such as the deformation energy for the collision of grinding balls (E_C – R1) and the angular speed (ω_D – R2) [37,39].

$$E_C = \frac{\left[7.66.10^{-2} \bullet R_d^{1,2} \bullet \rho^{0,6} \bullet E^{0,4}\right] \bullet d_b \bullet \omega_D^{1,2}}{\sigma} \tag{R1}$$

$$\omega_D = \frac{2 \bullet \pi \bullet n}{60} \tag{R2}$$

In these equations, the variable R_d represents the distance between the center of the disk to the second one (0.11 m), ρ denotes the density of the material of the milling balls (5730 g/cm³), E represents the modulus of elasticity of the material of the milling balls ($1{,}75.10^{11}$ Pa), d_b represents the diameter of the milling balls, σ reflects the surface density of the powder that was adhered to the milling balls (approximately 0.1 kg/m²), and n represents the rotations per minute value [37,39]. The calculated results are presented in Table 2.

Prepared powders were studied by diffraction methods. The X-ray diffraction (X'Pert3 Powder instrument in Bragg-Brentano geometry using a Cu anode - λ = 1.5418, V = 40 kV, I = 30 mA) was used for the determination of phase composition. The particle size distribution was measured by laser diffraction (MasterSizer 3000, Malvem Panalytical, UK). The powders were measured in liquid (water). The machine was equipped with a Hydro LV unit filled with distilled water dispersant, and the measured suspension was stirred at 3000 RPM. A built-in ultrasound unit was not used. It was found that its usage during measurement has negligible effect. Powders were measured by red and blue light of wavelengths 633 nm (He–Ne laser, 4 mW) and 470 nm (LED, 10 mW) each for 30 s. Data were evaluated in the Mastersizer 3000 v 3.50 software using the Fraunhofer scattering model.

The selected mechanically alloyed powders were then consolidated using the Spark Plasma Sintering (SPS) method (FCT System HP-D 10) under an argon atmosphere (purity 99.95 %) at a temperature of 300 °C and a pressure of 80 MPa for 10 min using a graphite die. The heating rate was set at 100 K/min. For comparison of the effect of the alloying elements, pure zinc powder was also sintered at similar conditions. The consolidated samples had a cylindrical shape with a diameter of 20 mm. These compacts were further processed by extrusion at 200 °C, 1 mm/

Table 2
Calculated angular speed and deformation energy based on milling parameters.

Size of milling balls [mm]	Angular speed ω_d [rad/s]	Deformation energy E_C [kJ]
5	84	311
10	84	622
15	84	933

min, and extrusion ratio (ER) equal to 10.

The designation of the selected alloys used throughout the paper and their processing parameters are listed in Table 3. The parameters for the mechanical alloying were selected with the aim of obtaining powders of fine-grained microstructure, desired particle size, low contamination, and a minimalized content of intermetallic phases. The conditions for spark plasma sintering were selected in agreement with our previous research [37,38].

2.2. Microstructure

The microstructure of the prepared materials was characterized using optical microscopy (Olympus PME3) and scanning electron microscopy (SEM – TESCAN VEGA 3 LMU) equipped with an EDX analyzer (OXFORD Instruments AZtec) and EBSD (OXFORD Instruments Aztec Crystal). Samples were first ground on SiC grinding papers (P400 – P2500), and subsequently polished using diamond paste D2 (UR-diamant) and Eposil Non-Dry suspension. For EBSD measurements samples were further electrochemically polished in solution ethanol and phosphoric acid in volume ratio 1:1. Stainless steel was used as a counter electrode and polishing was performed at a voltage of 4 V at −15 °C for approximately 10 min. After polishing, the samples were rinsed by ethanol and demineralized water. During the EBSD measurement, the binning was set to x4, accelerating voltage was 20 kV and current 32 nA. The step size was chosen to be 50 nm. EBSD analysis was performed using an FEI 3D Quanta 3D field-emission-gun DualBeam scanning electron microscope equipped with an EBSD detector TSL/EDAX Hikari. The phase composition was determined using X-ray diffraction. The size of the grains, intermediate phases and Si particles was evaluated using image analyses in combination with the results from SEM. The distances between the two parallel lines in the longest and shortest directions that restrict the object from its edges were evaluated and an average of these values for each grain, or intermetallic phase is subsequently presented. At least 200 measurements have been performed for all characterized components. Grain size was also measured by EBSD analysis. Results were presented as an equivalent diameter, which is a hypothetical measure representing the diameter of a particle as if it had a simple, cylindrical shape with the same characteristics. The microstructure details were examined using a transmission electron microscope (TEM—EFTEM Jeol 2200 FS, operating at an accelerating voltage of 300 kV, equipped with LaB6, Jeol GmbH, Tokyo, Japan). Initially, thin strips with a thickness of <100 μm were created through grinding and subsequently thinned using Gatan's PIPS polishing system with Ar ions (Gatan, Pleasanton, CA, United States).

2.3. Mechanical properties

Mechanical properties of materials were studied through measurements of hardness, tribology and tensile tests. Microhardness (HV1) was analyzed using a Future-Tech FM-100 machine with a load of 1 kg.

Tensile test were performed on universal mechanical test machine LabTest Instron 5882. Samples for tensile test were prepared only for extruded samples with cylinder shape. The specimens had a total length of 60 mm and specific dimensions are evident from the drawing (Fig. 1). Strain rate was set at 0.001 s^{-1}. Tribology tests were conducted using an oscillating method on TRIBOtester (Tribotechnic). The samples were first ground, polished (using diamond paste D2 and Eposil Non-Dry suspension), and cleaned with ethanol before the wear test. The parameters for the measurement were selected as: excentre = 5 mm, sliding speed = 10 mm/s, normal load = 1 N, sliding length = 20 m. An Al_2O_3 ball was used as the static partner.

2.4. Corrosion properties

In order to evaluate the corrosion behavior of the alloys, selected materials were exposed to Leibovitz medium L-15 (Biowest) simulating the conditions in human organisms, for a period of seven days. The medium contains both an inorganic component simulating the ionic aggressiveness of blood plasma and a biochemical component, including amino acids and vitamins. The comparison of key components concentration with other corrosion media is shown in Table 4). The buffering capacity of this electrolyte does not depend on the concentration of CO_2 in the atmosphere and was sufficient to maintain a constant pH of 7.4 throughout the whole exposure. The protein component was supplied in the form of an addition of 5 % fetal bovine serum, and resistance to microbial contamination was ensured by the addition of 1 % antibiotic/antimycotic solution (both from Sigma-Aldrich). The measurements were carried out at 37 °C in a PTFE cell with an o-ring between the cell and the vertically oriented sample. The materials were ground (FEPA P2500) and degreased with ethanol immediately before exposure. Electrochemical monitoring was performed using non-destructive techniques, including open circuit potential (EOC) and polarization resistance measurements (R_P, ±20mV/E_{OC}, scan rate 0.125 mV/s). A three-electrode setup was used with an Ag–AgCl reference electrode (3 mol/L KCl) and a glassy carbon counter electrode. Gamry Reference 600 potentiostat was used for the measurements. After exposure, the surface of the sample was washed with water, ethanol, dried, and then studied using the SEM.

3. Results

3.1. Powder analyses

In this study, powder mixtures were prepared under different process parameters as listed in Table 5. The processed powders were then compared based on their phase composition (XRD diffraction) and particle size. The results indicate that various parameters of milling (time, and size of the milling balls) significantly affect the refinement of the powder particles. An increase in milling time leads to a significant refinement of the powder particles due to the increased number of collisions between powder particles and milling balls, which results in the breaking of particles into smaller pieces. The results of the laser diffraction are listed in Table 5 and Fig. 2. $D_V(50)$ percentile value represents the median of particle sizes obtained during particle size measurement. The XRD analyses (Fig. 3) indicate the presence of the
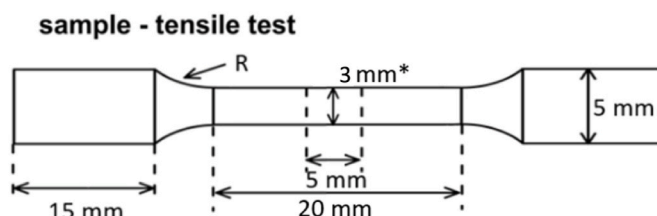
Table 3
Designation of studied materials according to their processing conditions.

Marking	Chemical composition	Mechanical alloying	SPS	Extrusion
Zn^{SPSa}	Zn	–	300 °C, 80 MPa	–
Zn–1Mg^{SPS}	Zn–1Mg	800 RPM, 8 h, 15 mm	300 °C, 80 MPa	–
Zn–1Mg$^{SPS + Ex}$	Zn–1Mg	800 RPM, 8 h, 15 mm	300 °C, 80 MPa	ER 10, 200 °C
Zn–1Mg–1Si^{SPS}	Zn–1Mg–1Si	800 RPM, 8 h, 15 mm	300 °C, 80 MPa	–
Zn–1Mg–1Si$^{SPS + Ex}$	Zn–1Mg–1Si	800 RPM, 8 h, 15 mm	300 °C, 80 MPa	ER 10, 200 °C

[a] Spark Plasma Sintering performed on commercial zinc powder (99.9%, particle size <149 μm, Thermo Fisher Scientific).

Fig. 1. Sample – Tensile test.

Table 4
Ion concentration in corrosion media simulating human blood plasma.

c [mmol/l]	Na$^+$	K$^+$	Mg^{2+}	Ca^{2+}	Cl$^-$	HCO$_3^-$	HPO$_4^{2-}$	H2PO$_4^{2-}$	SO$_4^{2-}$	Others
Blood plasma	142	5	1.5	2.5	103	27	1	–	0.5	Amino acids, Vitamins, Proteins
PS (ISO 10993-15)	154	–	–	–	154	–	–	–	–	–
PBS (ASTM F2729)	157	4.46	–	–	139.7	–	10	1.76	–	–
SBF27 (Muller&Muller)	142	5	1.5	2.5	103	27	1	–	0.5	–
DMEM	155.3	5.3	0.8	1.8	119.3	44	0.9	–	0.8	A. C., V.
EMEM (Sigma M7278)	121.7	5.4	0.8	1.8	103.1	26.2	0.7	–	0.8	A. C., V.
L15 (Biowest L0300)	136.9	5.8	1.8	1.3	141.4	–	1.3	0.4	0.8	A. C., V.

Table 5
Powder characteristics after mechanical alloying.

Composition	Milling time [h]	Size of milling balls [cm]	$D_V(50)$ [µm]
Zn	–	–	110.0 ± 1.6
Zn–1Mg–1Si	0.5	1	175.0 ± 2.5
	1	1	91.3 ± 2.0
	2	1	71.7 ± 1.8
	4	1	56.4 ± 1.8
	8	0,5	45.1 ± 2.2
	8	1	68.7 ± 2.8
	8[a]	1,5	76.7 ± 2.6
Zn–1Mg	8[a]	1,5	–

[a] Selected parameters for further material processing.

Mg$_2$Zn$_{11}$ intermetallic phase in prepared powders. We observed that the increase in milling time leads to an increase in the solubility of magnesium in the zinc matrix. After 4 h of milling, the content of the Mg$_2$Zn$_{11}$ phase was 4 wt % while after 8 h of milling, it was even below 1 wt %. Silicon, on the other hand, does not form any phases with zinc. The combination of magnesium and silicon could potentially lead to the formation of the Mg$_2$Si phase, but this phase was not identified by selected analyses. An 8 h of milling led to the finest powders with the most homogenous particle size distribution. The selected size of balls equal to 1.5 cm generated the highest deformation energy, which supported the process of mechanical alloying and led to the dissolution of the magnesium in the zinc matrix. Increased solubility was also observed for the smallest (0.5 cm in diameter) milling balls due to a higher amount of collisions during milling. However, an increased number of milling balls (to preserve a 1:5 powder-to-ball weight ratio) resulted in the contamination of powders by ZrO$_2$. The same impurities were observed for milling with 1 cm in diameter. Based on the results, the parameters combining the longest milling time and largest milling balls were selected for further material processing.

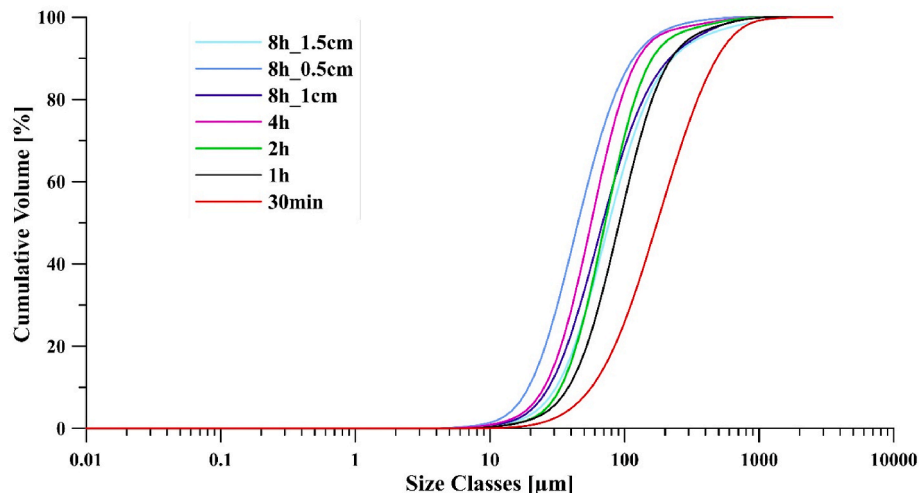The chemical composition of the prepared powders was verified by X-ray fluorescence analysis and EDS analysis. The results are listed in Table 6. Minor deviation from planned composition (Zn–1Mg, Zn–1Mg–1Si) is related to the material losses of the Zn on the milling vessels and balls.

The phase composition of compacted materials Zn, Zn–1Mg, and Zn–1Mg–1Si, which were prepared using SPS or a combination of SPS and extrusion, are presented in Fig. 4 and Table 7. These results indicate that the phase composition of compacted materials is not affected by the compaction technique in relation to the mechanically alloyed powders.

3.2. Microstructure

Powders with compositions of Zn, Zn–1Mg, and Zn–1Mg–1Si were compacted using SPS. The prepared materials were characterized by a fine-grained microstructure with an oxide shell remaining on the surface of the original powder particles (Fig. 5). Both Zn–1Mg (Fig. 5A) and Zn–1Mg–1Si (Fig. 5B) alloys displayed a fine, homogenous microstructure with minimal porosity. The microstructure was dominated by equiaxed with the equivalent diameter below 1 µm. Silicon was preserved in the pure form with a wide range of particle size (ranged from 300 to 3000 nm with the peak values of particle size distribution close to 730 nm, Fig. 5B, white arrows) without the formation of any kind of intermediate phases or the tendency to dissolve in the zinc matrix.

The distribution of elements in the Zn–1Mg–1Si alloy prepared by spark plasma sintering (SPS) is shown in Fig. 6. Magnesium is homogeneously distributed throughout the sample in the form of a solid solution in Zn or fine intermetallic phases (Mg$_2$Zn$_{11}$). Silicon is observed as partially rounded particles that are rather randomly distributed within the bulk material. However, the local concentration of particles may slightly differ which decreases the overall material inhomogeneity.

The microstructure of samples prepared by a combination of spark plasma sintering (SPS) and extrusion are displayed in Figs. 7–9. These results are further supported by EBSD analyses (Figs. 11 and 12) enabling confirmation of the grain size and orientation. During the
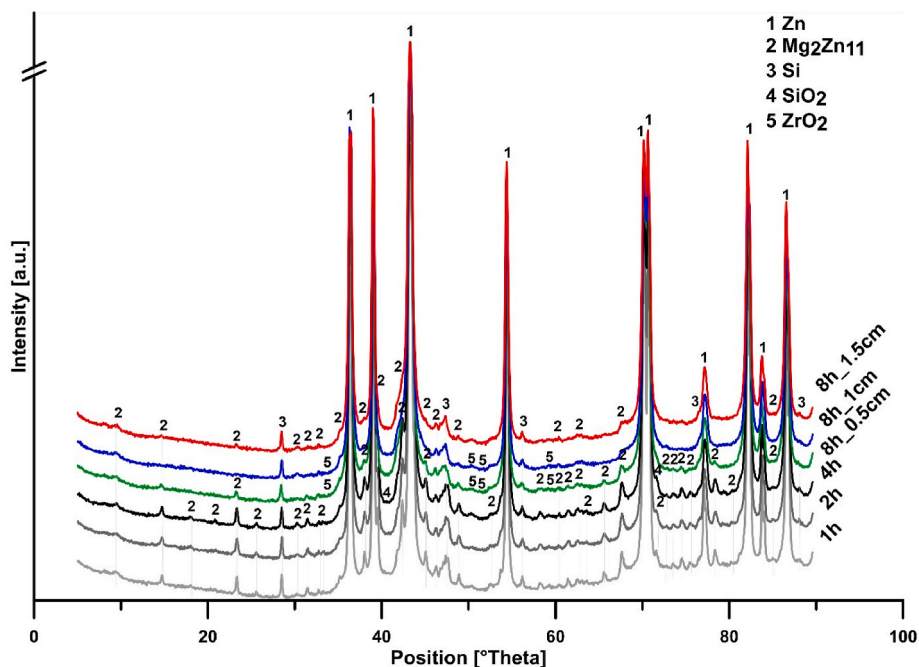

Fig. 2. Particle size distribution of powders after mechanical alloying.

Fig. 3. The X-ray diffractogram of powders prepared by mechanical alloying.

Table 6
Chemical analyses of prepared powders - X-ray fluorescence.

Composition	Zn (wt. %)	Mg (wt. %)	Si (wt. %)
Zn–1Mg	98.8	1.2	–
Zn–1Mg–1Si	97.4	1.1	1.5

extrusion process the oxide shells are partially broken and intermetallic phases (Mg_2Zn_{11}), oxide particles redistributed and arranged in rows parallel to the extrusion direction (ED). The fine oxides generated by the deformation of oxide shells and the once formed as in-situ oxide particles during mechanical alloying were spread within the material,

primarily at the grain boundaries (Fig. 7 - white arrows, Fig. 9 – white particles). Contrary to the zinc matrix and Mg_2Zn_{11}, pure silicon did not show any deformation or refinement during extrusion (Fig. 8) and therefore achieved a similar particle size (peak values of particle size distribution close to 700 nm) in extruded material like in the material prepared by SPS. Overall, the microstructure of the extruded materials was slightly different. The grain size evaluated from EBSD measurements in the plane parallel to the extrusion direction ranged from 148 to 646 nm (249–867 nm) with the peak values of grain size distribution close to 397 nm for Zn–1Mg–1Si (558 nm for Zn–1Mg), respectively (Fig. 10). For both materials, slightly elongated grains in the extrusion direction were observed indicating some deformation and stress
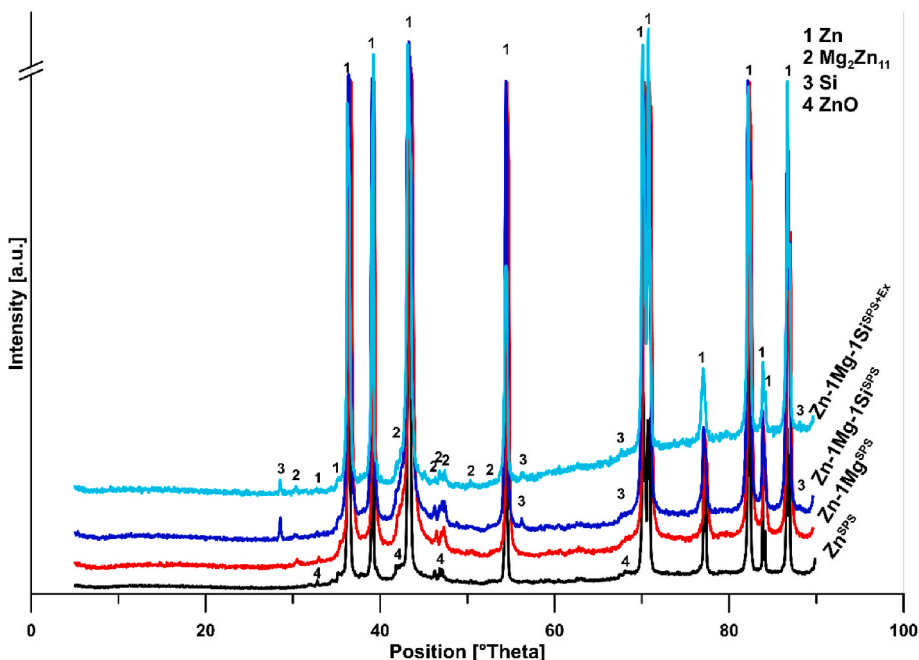

Fig. 4. The X-ray diffractogram of compacted samples.

Table 7
Phase composition of studied materials after compaction by SPS and extrusion.

Materials	Processing	Zn	Mg$_2$Zn$_{11}$	Si
Zn	SPS	100	–	–
Zn–1Mg	MA + SPS	100	<1	–
Zn–1Mg–1Si	MA + SPS	98	1	1
	MA + SPS + Ex	98	1	1

preserved in the material. Materials also locally contained grains of higher size (several micrometers), which were coarsen due to the increased temperature during extrusion and insufficient number of obstacles (oxide particles, intermetallic phases, Si) in specific areas restricting the grain growth. Grains in extrusion direction could locally have up to 3 μm in length, in perpendicular direction up to 0.8 μm. Further analysis of Zn–1Mg alloy by TEM (Fig. 9) showed the existence of small oxide particles at grain boundaries, suggesting the positive effect on the lower grain size. These particles contained also increased amount of Mg compared to the matrix. Therefore, we expect that material contains both MgO and ZnO oxides.

EBSD measurements have been used to analyze the grain size and orientation of the zinc matrix (Figs. 11 and 12). The non-indexed points (black areas) reflect the remaining phases presented in the microstructure. Obtained results indicated the weak texture of processed materials which is not generally observed for extruded zinc alloys. The main components were {0001}, {10-10} and {10–12} fiber textures.

3.3. Mechanical properties

The mechanical properties of prepared materials were evaluated using Vickers hardness measurements (HV1) and tensile tests. The results of the tensile tests are presented in Fig. 13, with one tensile curve shown as a representative. Three measurements were performed for all materials and are used in statistical results. The obtained data were evaluated in the form of average values and standard deviations (Table 8.)

The addition of alloying elements, in combination with grain refinement, led to the improvement of the hardness of studied materials compared to the pure zinc. Results showed significant increase in HV from 44 ± 1 HV1 (Zn) to 129 ± 2 HV1 (Zn–1Mg prepared by combination of mechanical alloying and spark plasma sintering). Addition of

silicon or further extrusion of SPSed products didn't improve hardness of the material significantly. The effects of extrusion on the tensile mechanical properties of selected alloys are further listed in Table 8. Significant improvement in the TYS (tensile yield strength), UTS (ultimate tensile strength) was observed. TYS and UTS increased from 74 ± 2 and 109 ± 5 MPa for zinc to 227 ± 6 and 412 ± 4 MPa for Zn–1Mg, respectively and to 296 ± 24 and 422 ± 12 MPa for Zn–1Mg–1Si. However, the plasticity of materials observed during tensile tests is reduced for extruded materials (Fig. 13) probably due to the redistribution of oxides and Si in the microstructure. Elongation of extruded alloys reached 2.0 ± 0.2 % for Zn–1Mg and 1.8 ± 0.6 % for Zn–1Mg–1Si. Obtained results also indicate that there is only a minor effect of silicon addition on the measured mechanical properties of extruded Zn–1Mg.

3.4. Tribological properties

The tribological properties of the prepared Zn and its alloys were measured on a pin-on-disc tribometer with an Al$_2$O$_3$ ball. The results describing abrasion during wear are the friction coefficient, track area, and average wear rate, (Table 9). All measurements show an intense increase in the friction coefficient at the beginning of the measurements, due to the damage to the surface oxide layer. After a few seconds, the values stabilized (as visible in Fig. 14). The average value is listed in Table 9. The presented results indicate a significant effect of the material's microstructure conditions on the tribological properties. The selected materials show lower hardness than Al$_2$O$_3$, leading to adhesive wear and distortion of the surface of the alloy, followed by metal fragments breaking off and sticking to the surface of the test ball. After the breakage of the oxide layer and contamination of the surface of the Al$_2$O$_3$ ball, the mechanism of wear changed to an abrasive one.

The results of wear testing indicate that materials were plastically deformed, leading to the formation of grooves (as depicted in Fig. 15). A comparison of pure Zn to the Zn–1Mg alloy prepared by SPS and SPS + Ex revealed differences in track morphology. Pure zinc (Fig. 15A) was covered by visible local particles that were generated by the accumulation of zinc oxides during the movement of the Al$_2$O$_3$ ball and were primarily located at the ends of the track. Larger particles located in the center of the track were probably released from the surface of the Al$_2$O$_3$ ball in the last stage of the measurement.

The results in Table 9 document a positive effect of Mg$_2$Zn$_{11}$ intermetallic phases on the increased wear resistance in Zn–1Mg^{SPS}.
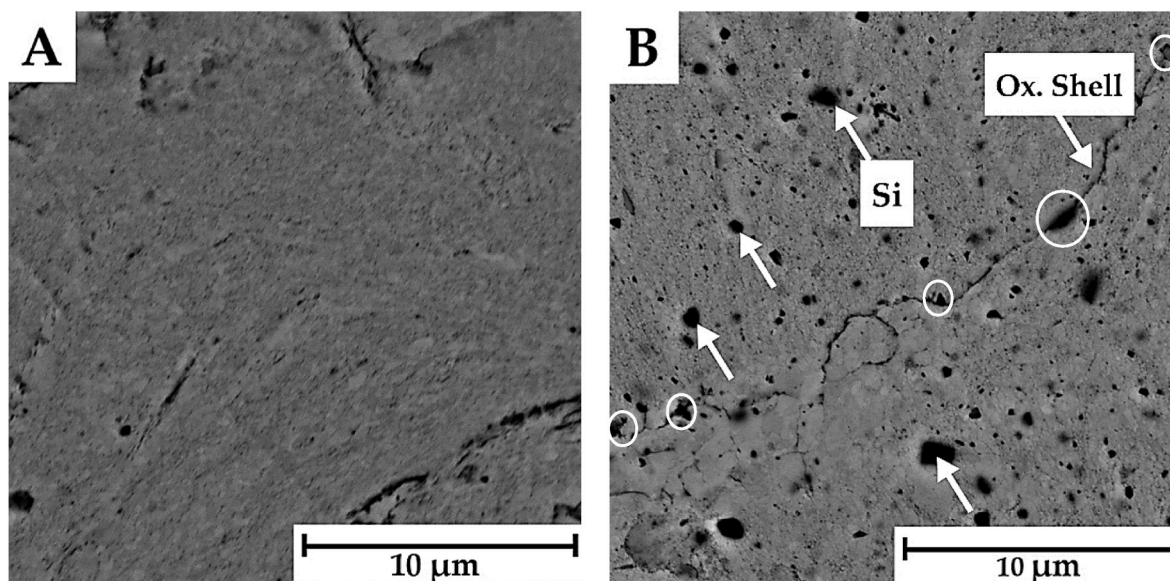

Fig. 5. The microstructure of prepared samples (Scanning electron microscopy): A) Zn–1Mg^{SPS}, B) Zn–1Mg–1Si^{SPS}. The black particles in white circles represent the Si-disrupting oxide shells that remain on the surface of the original powder particles.
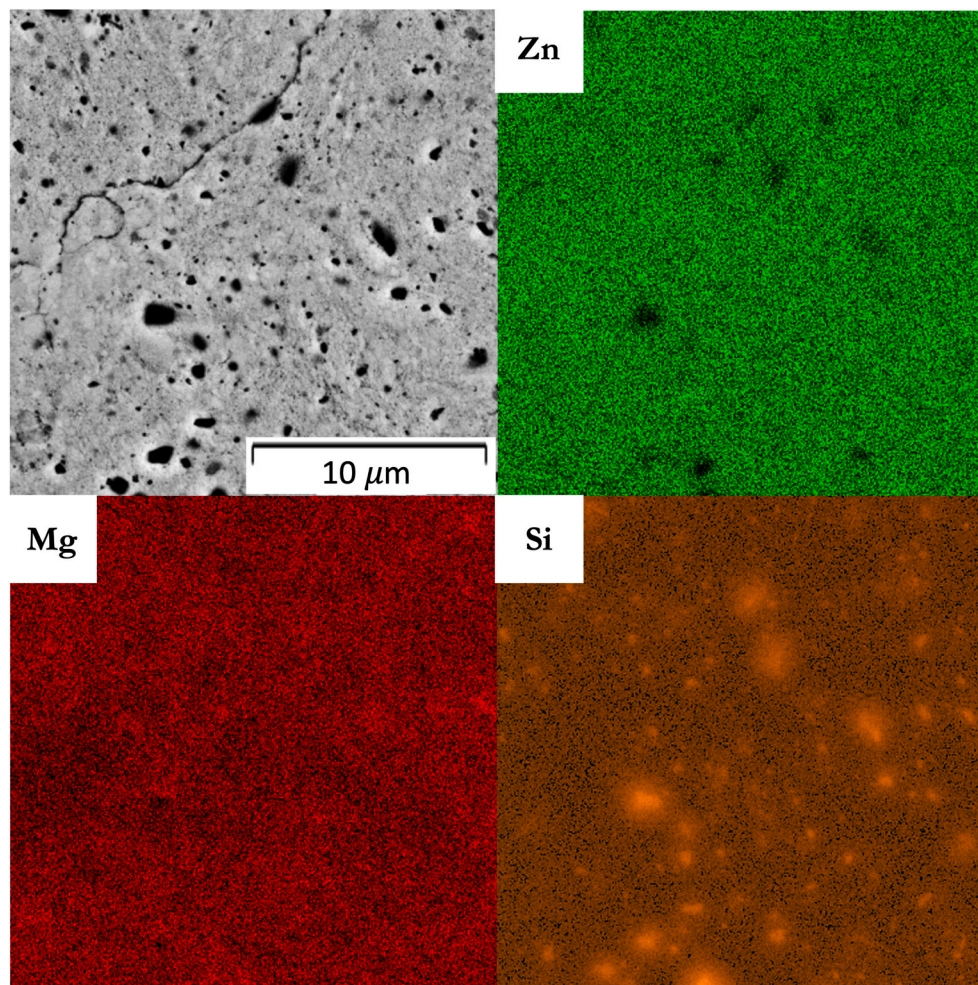
Fig. 6. Distribution of elements in Zn–1Mg–1Si alloy prepared by SPS (Scanning electron microscopy-Energy dispersive spectroscopy).
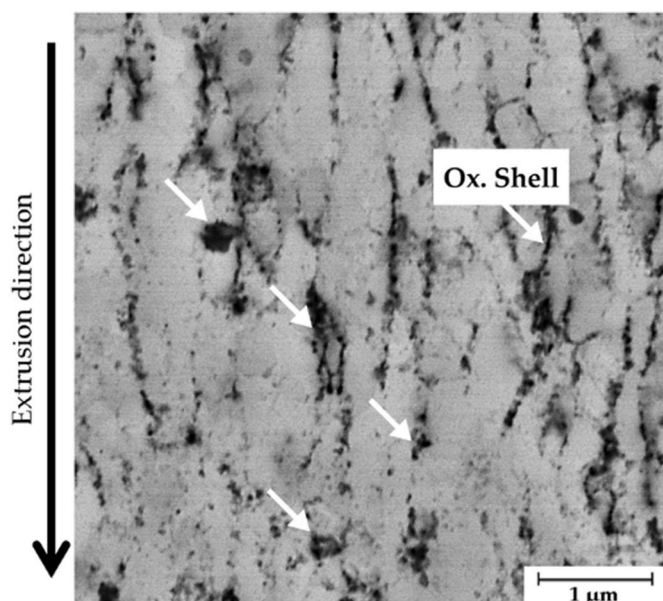

Fig. 7. Microstructure of Zn–1Mg alloy prepared by SPS and extrusion – displayed in the longitudinal plane parallel to the ED (Scanning electron microscopy).

Furthermore, there is a difference in the morphology of tracks for Zn–1Mg^{SPS} and Zn (Fig. 15). Figs. 15B and **16** indicates bonded layers of oxides that are almost continuously distributed throughout the entire center of the track for Zn–1Mg^{SPS}. It is suggested that all original powder particles with oxide shells on their surface in the material are ripped out of the surface by the Al$_2$O$_3$ ball and subsequently deployed and deformed on the surface of the track, which leads to an overall increase in the friction coefficient and decrease of wear rate (Table 9). A similar effect of oxides on friction coefficient was described by Guezmil et al. [40], where different thicknesses of surface oxidation on anodized Al5754 aluminum alloy were compared.

Fig. 15C (Zn–1Mg$^{SPS + Ex}$) appears to be similar to pure zinc, indicating a significant effect of extrusion on tribological behavior. Breaking the oxide shells into finer and individual particles is suggested to prevent the bonding of oxides on the surface (Fig. 16). The addition of silicon led to the generation of similar tracks (Fig. 15D) for Zn–1Mg$^{SPS + Ex}$ although slightly higher wear rate and lower friction coefficient. This is attributed to the release of Si particles during wear measurement, while these particles further work as an abrasive medium increasing the wear rate.

3.5. Corrosion properties

Corrosion behavior was estimated based on the 7-day immersion tests. In terms of the open circuit potential (Fig. 17A), all materials are quite comparable for the first 3 days, with potentials below - 1.1 V/ SSCE; around day 4, both the silicon-doped alloys and the non-extruded
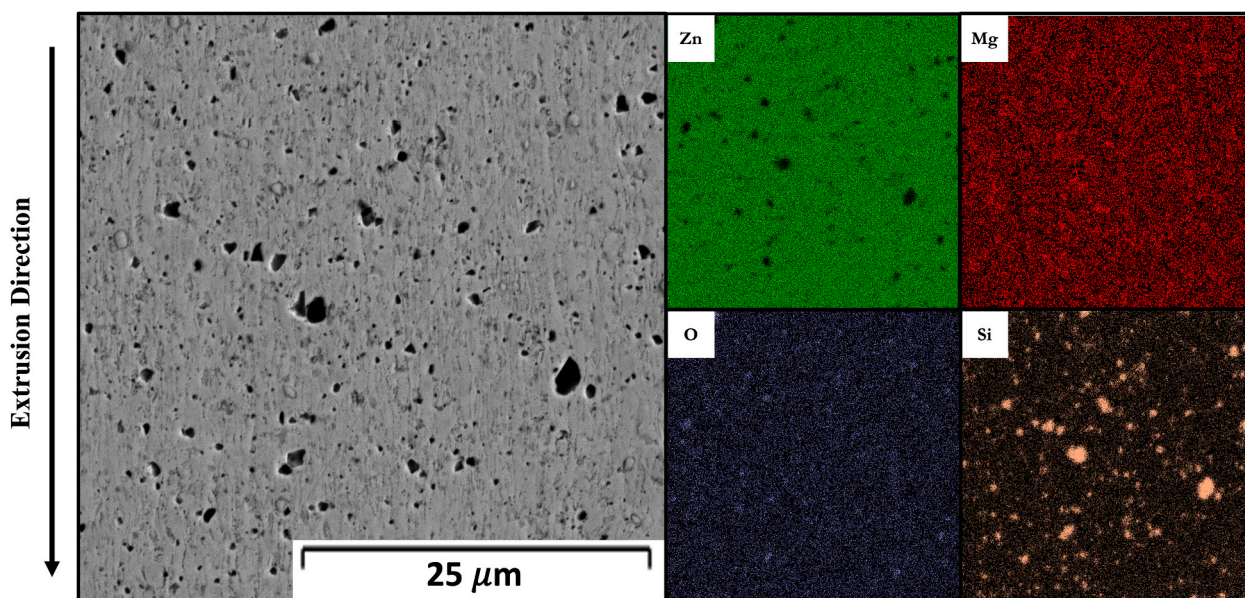
Fig. 8. The distribution of elements in Zn–1Mg–1Si alloy prepared by SPS and extrusion (Scanning electron microscopy-Energy dispersive spectroscopy).

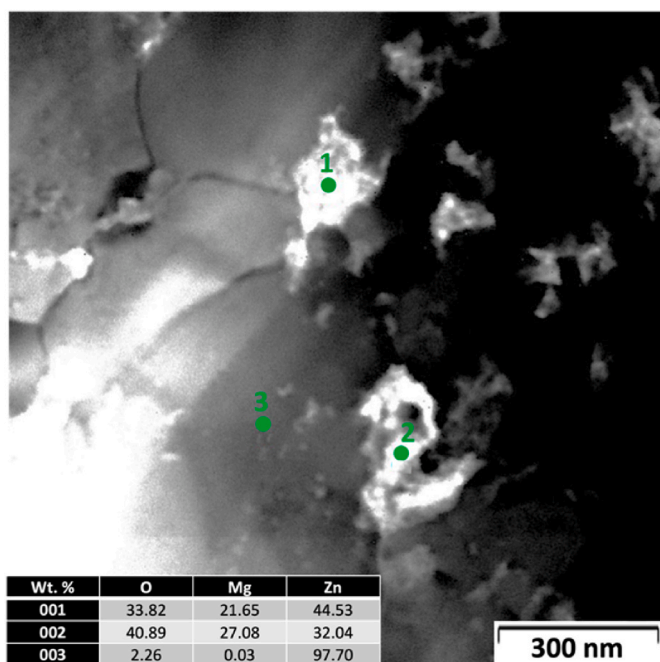| Wt. %	O	Mg	Zn
001	33.82	21.65	44.53
002	40.89	27.08	32.04
003	2.26	0.03	97.70

Fig. 9. The detail of the microstructure of the Zn–1Mg alloy prepared by SPS and extrusion (Transmision electron microscopy-Energy dispersive spectroscopy).

Fig. 10. Grain size distribution of Zn–1Mg and Zn–1Mg–1Si prepared by combination of SPS and extrusion.

binary alloy exhibited a sharp increase of 0.18 V to approximately the standard zinc potential (−0.97 V/SSCE) and stabilized at this value. This trend is followed by the Zn–1Mg$^{(SPS + Ex)}$ alloy over the next day. This change did not occur for the pure zinc prepared by SPS. Due to the considerable hydrogen overvoltage on zinc and the Mg$_2$Zn$_{11}$ phase, oxygen depolarization can be expected as the dominant cathodic reaction even in the initial exposure phase [41]. Changes in the open circuit potential are preceded by several hours by changes in the trend of the polarization resistance, which again increases for the alloys. The effect of the sample preparation method is evident here, where the increase is approximately two or three times for materials prepared by SPS only but is of the order of magnitude for alloys subjected to subsequent extrusion.
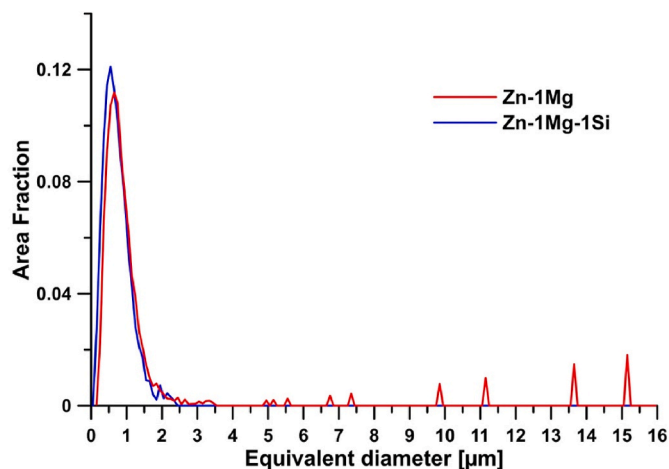
The polarization resistance was approximately 0.1 Ω m^2, which, when converted (using the Stern-Geary coefficient of 0.026 mV) to a uniform corrosion rate, corresponds to 0.4 mm per year. These values in the final exposure phase are 0.5 mm/y for Zn^{SPS}, 0.2 mm/y for Zn–1Mg^{SPS}, 0.1 mm/y for Zn–1Mg–1Si^{SPS}, 0.03 mm/y for Zn–1Mg$^{SPS + Ex}$ and 0.05 mm/y for Zn–1Mg–1Si$^{SPS + Ex}$.

From a macroscopic view (Fig. 17B), all materials prepared by SPS corroded over almost the entire surface. The less attacked areas were located below the O-ring. A detailed view shows that dissolution occurred primarily along the boundaries of the oxide envelopes. Fibrous deposits of probable protein origin are evident on the magnesium-containing samples. In the samples with subsequent extrusion, the surface was mostly covered by a uniform layer of corrosion products, however, at the interface with the PTFE holder, fibrous deposits were evident, and a distinct layer replicating the original surface morphology was observed in their vicinity.

The EDS analysis (Table 10) showed that in all cases there was a significant increase in carbon and oxygen - more than three times higher values than in the unexposed surface. Furthermore, alloying elements - especially silicon - are presented on the corroded surface in a higher
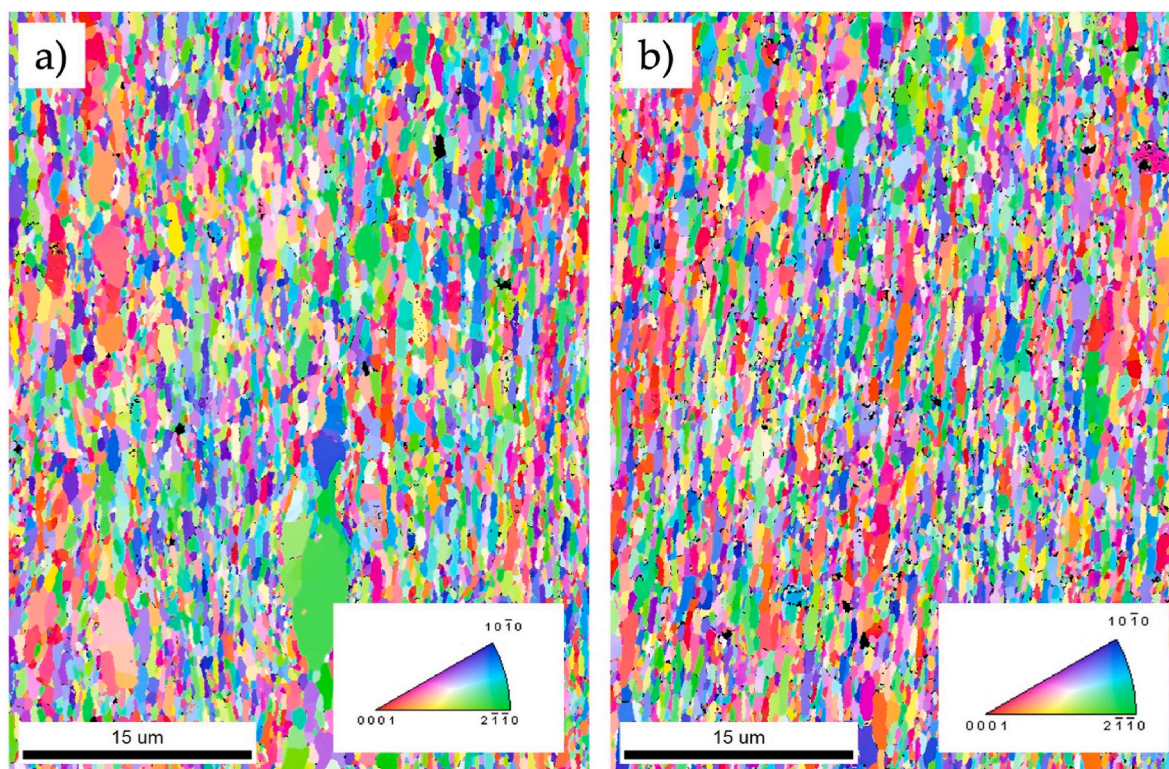
Fig. 11. The IPF maps of material prepared by SPS and extrusion: a) Zn–1Mg$^{SPS + Ex,}$ b) Zn–1Mg–1Si$^{SPS + Ex}$.
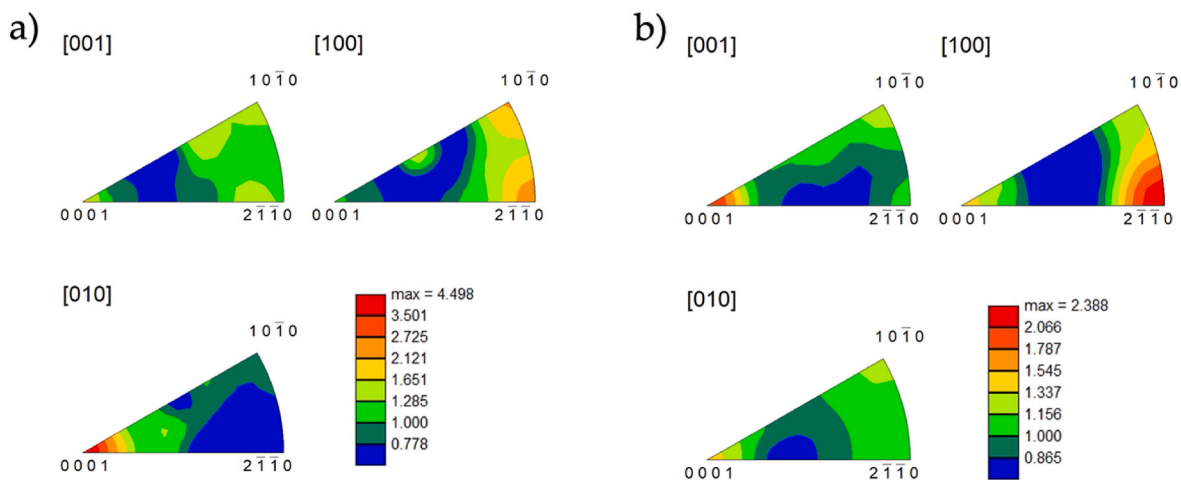

Fig. 12. The IPF plots of material prepared by SPS and extrusion: a) Zn–1Mg$^{SPS + Ex}$, b) Zn–1Mg–1Si$^{SPS + Ex}$.

proportion. Phosphorus and calcium are also presented in the surface layer (i.e. elements occurring mainly on the bone tissue side during *in-vivo* exposure), but their ratio indicates the presence of phosphates other than calcium apatite, which is consistent with the characteristics of the corrosion products of zinc alloys *in-vivo* [42]. Away from the surface, i.e. on fibrous deposits, the Ca/P ratio increases. The layer around the fibrous deposits on the extruded materials shows a decrease in magnesium and calcium content, and to a lesser extent phosphorus, and higher amounts of chlorine.

4. Discussion

4.1. Powder analyses and microstructure

The results of the X-ray diffraction (XRD) analyses revealed that the mechanical alloying of Zn–1Mg–1Si led to the precipitation of the Mg_2Zn_{11} intermetallic phase. Similar results have been also observed in previous work dealing with Zn–Mg binary alloys [37], however in the presented study we pushed the milling parameters towards higher deformation energy necessary for preparation of non-equilibrium microstructure conditions (e.g. extended solubility of alloying elements in Zn). The powder particle size was affected significantly by the dimensions of milling balls (Table 5) with the lowest particle size after milling with balls 0.5 cm in diameter. Furthermore, the particle size of
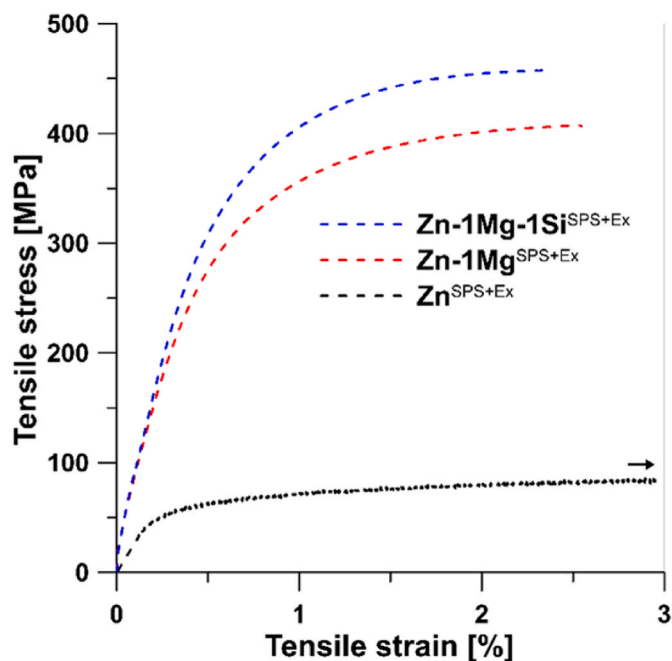
Fig. 13. Engineering stress-strain diagrams of studied materials.

Table 8
Results of mechanical properties measurements.

Comp.	$\sigma_{TYS\ 0,2}$ [MPa]	σ_{UTS} [MPa]	Elongation [%]	HV1
Zn^{SPS}	–	–	–	44 ± 1
Zn–1Mg^{SPS}	–	–	–	129 ± 2
Zn–1Mg–1Si^{SPS}	–	–	–	130 ± 2
Zn$^{SPS\ +\ Ex}$	74 ± 2	109 ± 5	18.3 ± 4	
Zn–1Mg$^{SPS\ +\ Ex}$	227 ± 6	412 ± 4	2.0 ± 0.2	135 ± 3
Zn–1Mg–1Si$^{SPS\ +\ Ex}$	296 ± 24	422 ± 12	1.8 ± 0.6	137 ± 2

Table 9
Tribological properties of Zn, Zn–1Mg, and Zn–1Mg–1Si materials prepared by SPS and extrusion.

Sample	HV1	Average wear rate [mm³/N·m]	Track area [µm²]	Friction coefficient
Zn^{SPS}	44 ± 1	(13.2 ± 0.9)·10³	(53.8 ± 3.6)·10³	0.84 ± 0.03
Zn–1Mg^{SPS}	129 ± 2	(4.7 ± 0.5)·10³	(18.6 ± 2.2)·10³	1.04 ± 0.02
Zn–1Mg–1Si^{SPS}	130 ± 2	(4.1 ± 0.5)·10³	(16.4 ± 1.1)·10³	0.95 ± 0.01
Zn–1Mg$^{SPS\ +\ Ex}$	135 ± 3	(6.5 ± 1.3) ·10³	(26.1 ± 5.2)·10³	0.97 ± 0.07
Zn–1Mg–1Si$^{SPS\ +\ Ex}$	137 ± 2	(10.7 ± 0.8)·10³	(42.8 ± 2.7)·10³	0.86 ± 0.01

the prepared powders decreased hyperbolically with milling time from 0.5 to 4 h. A similar trend in particle size distribution was observed for Mg–2Zn and Mg–27Zn prepared by mechanical alloying [43]. On the contrary, a milling time of 8 h led to the increased particle size due to the prevailing effect of cold joining. Effect of powder size on mechanical and corrosion properties was studied by Li et al. [44] on $Mg_{66}Zn_{30}Ca_4$ bio glasses prepared by SPS, which authors observed positive effect of finer powders on higher compressive strength. The similar conclusion was presented by Krystýnová et al. [45], who studied pure zinc prepared by powder metallurgy using hot isostatic pressing (HIP). Also, the distribution of alloying elements and intermetallic phases in the microstructure was significantly affected by milling conditions. The content of Mg_2Zn_{11} decreased from 4 to 1 wt % for powder milled for 4 and 8 h,

respectively. Such results indicate that using mechanical alloying, part of the Mg entered the zinc matrix and existed in the form of a solid solution as described already for the preparation of meta-stable alloys [46, 47]. Besides, Mg has a high tendency to form MgO, so part of it is incorporated in the oxide shells of powder particles furthermore, some dispersed oxides are formed due to the reaction of Mg with residual oxygen in Ar or the oxygen absorbed on the surface of the powder particles. Silicon remained always in the form of fine particles in the zinc matrix. These particles were oxidized on their surface.

It is worth mentioning that impurities such as ZrO_2 were generated by the friction of the milling vessel's walls and milling balls. The use of milling balls with a larger size (diameter = 1.5 cm) decreased the contamination due to a lower amount of impact between components (fewer grinding balls at a similar weight ratio to milled powder).

The selected methods and parameters of mechanical alloying were found to be effective for the preparation of nano-grained materials (Zn–1Mg and Zn–1Mg–1Si). The intensive deformation energy generated by mechanical alloying led to intensive grain refinement (grain size in hundreds of nm). Furthermore, SPS as a fast compaction technique was selected to maintain the fine-grained microstructure, however extrusion led to some extent to the grain size and shape redistribution. As a consequence, the material Zn–1Mg–1Si prepared by mechanical alloying (8 h), SPS and extrusion was characterized by the smallest observed average grain size (peak values of grain size distribution close to 397 nm), which represents a significantly reduced value compared to the Zn–1Mg alloy prepared by high-energy milling for a shorter time of 1 h with subsequent compaction by SPS (618 nm) [37]. Although there was observed local grain coarsening inside the microstructure of Zn–1Mg alloy, the majority of these coarsen areas contained still grains about 1 µm in size and their content was rather small, assuming they had no adverse effect on material properties. Occasionally larger grains were presented in the microstructure. Their existence is attributed to the inhomogeneous distribution of fine dispersed oxide particles in these regions leading to the limited blocking of grain boundaries and concomitant coarsening of the grains. This local coarsening was not observed for Zn–1Mg–1Si alloy due to the increased amount of blocking particles in the form of Si reinforcements.

It is known that thermomechanical processing of zinc alloys leads generally to grain refinement although, it is difficult to obtain grains sizes lower than several micrometers due the easy coarsening of Zn-based materials like in the case of Zn-0.4Mn-0.8Li prepared by hot rolling with grain size up to 2 µm [13] or Zn-0.8Mg-0.2Sr prepared by extrusion with grain size up to 2.1 µm [16]. It's worth mentioning that even using methods of intensive plastic deformation, such as Equal Channel Angular Pressing and High-Pressure Torsion was insufficient to reach similar values of grain sizes, indicating the average grain size of 2 µm [48] and 590 nm [49], respectively. On the contrary, the overall high homogeneity of the materials prepared in this study was negatively affected by the surface oxides on the original powder particles, which were transferred after compaction by SPS into a net of oxide shells throughout the whole material. The negative effects of these structures (intercrystalline fracture, lower elasticity of materials, etc.) were discussed in our previous research [37,38]. Our purpose was to partially prevent these conditions by further thermomechanical processing using extrusion. This enables to redistribution of these shells into finer particles inside the structure that could act as reinforcement, resulting in a composite-like material with improved properties (Fig. 8).

Various zinc-based composite materials have been studied, although they generally suffer from an inhomogeneous distribution of fine reinforcements. Gao et al. [27] studied zinc combined with different amounts of SiC (50 nm in size). The mixture of zinc and carbide was mechanically milled for 2 h at 250 RPM, which generated a layer of SiC on the surface of Zn particles. The prepared powders were compacted by selective laser melting. When the authors compared the microstructure of pure zinc with the prepared composite, they observed a significant decrease in grain size from 250 µm for Zn to 15 µm for Zn–2SiC. This
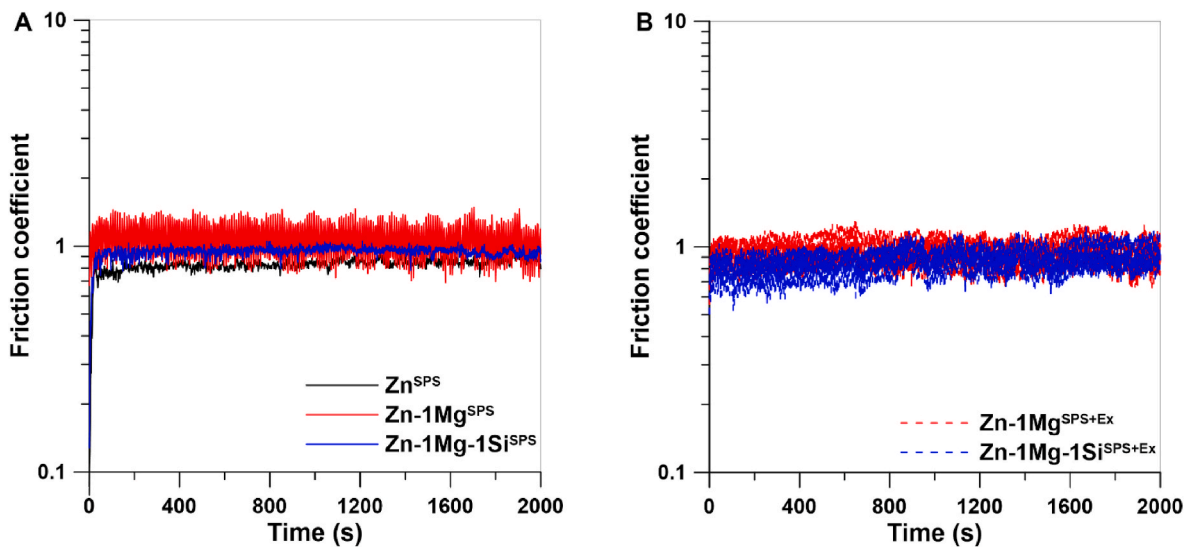
Fig. 14. Time dependence of friction coefficient during wear test: A) Materials prepared by SPS, B) Materials prepared by SPS and extrusion.
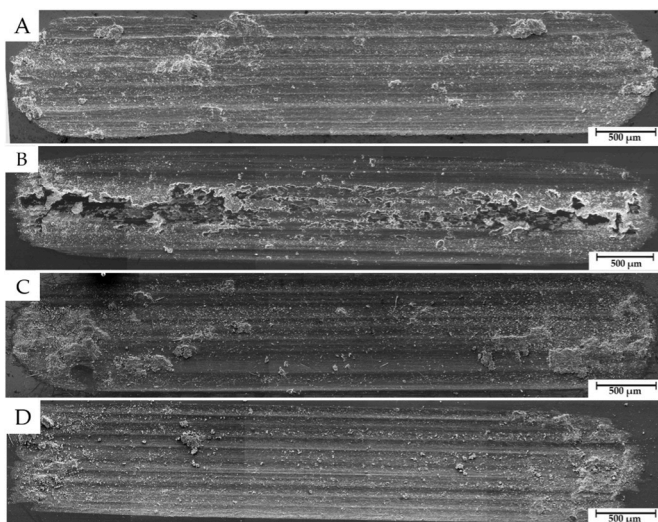

Fig. 15. Track after wear tests (Scanning electron microscopy): A) Zn, B) Zn–1Mg^{SPS}, C) Zn–1Mg$^{SPS + Ex}$, D) Zn–1Mg–1Si$^{SPS + Ex}$.

suggests that the addition of carbide promotes heterogeneous nucleation and blocks the grain growth in heat affected zone. Similar conclusions are suggested in the presented work although the suppression of grain growth by the presence of oxides particles is even stronger. Unfortunately, we did not observe further effects of silicon, probably due to the relatively coarse character of these particles. Another study of a zinc composite prepared by milling and SPS was published by Yang et al. [50]. In this work a zinc-hydroxyapatite (Zn-HA) material was prepared by milling for 1 h at 300 RPM and then compacting using sintration at a temperature of 380 °C, a pressure of 40 MPa, and a time of 6 min. The microstructure of the prepared composite contained hydroxyapatite concentrated on the edges of the original zinc particles, leading to a net structure like oxide shells in our alloys, deteriorating further material properties.

Various zinc-based alloys containing Mg as the main alloying element have been prepared by casting and extrusion (Zn-0.8Mg-0.2Sr [16,51], Zn–1Mg [22], and Zn-1.2 Mg [52], etc.). These materials are distinguished by different microstructures with grain sizes higher than 2 μm and rather coarse intermetallic phases (≈1–10 μm in size) arranged in rows parallel to the extrusion direction. For example, in

Zn-0.8Mg-0.2Sr alloy, Mg_2Zn_{11} and $ZnSr_{13}$ phases (1–3 μm in size) were arranged in rows 5–15 μm apart from each other [16]. On the contrary, materials presented in this study achieved significantly finer microstructure with grain size below 1 μm and size of homogeneously distributed intermediate phases even below 500 nm. Furthermore, the extrusion caused partial disruption of the oxide shell making other oxide particles useful for blocking grain growth while not affecting other microstructural characteristics compared to the products of SPS.

Interesting results were observed in the case of material texture after extrusion. Both Zn–1Mg and Zn–1Mg–1Si were characterized by several texture components like {0001}, {10-10} and {10–12} fiber textures. However, very weak texture was observed. It is known that zinc-based alloys prepared by extrusion are in the majority cases characterized by strong basal texture with basal planes oriented parallel to the extrusion direction. This is related to the dominance of basal slip during the deformation of materials leading to the reorientation of basal planes to the position parallel with extrusion direction. Besides, the $\langle 10\overline{1}0 \rangle$ and $\langle 10\overline{1}2 \rangle$ crystallographic directions are often aligned closely to the extrusion direction, which is associated with a non-basal slip in the prismatic slip system [53–55]. Week texture is a bit surprising because the grains are slightly elongated in the extrusion direction, which is generally also related to the preferential reorientation of grains, and therefore, stronger texture formation.

4.2. Mechanical properties

The presented results in Fig. 13 and Table 8 illustrate a compelling enhancement in mechanical properties, particularly strength values, through a combination of mechanical alloying, spark plasma sintering (SPS), and extrusion. The Zn–1Mg alloy, prepared using these techniques, exhibited an increase in ultimate tensile strength (UTS) compared to pure zinc. The addition of silicon as a reinforcing element further improved the alloy's strength, reaching a maximum value of 422 ± 12 MPa for the Zn–1Mg–1Si composite. The heightened strength in these materials can be attributed to several factors. Primarily, mechanical alloying induced significant grain refinement. Subsequently, the breaking of oxidic shells, formed during SPS compaction, by extrusion led to a formation of oxide particles that acted as reinforcement and barriers for dislocation slip, similarly as addition of silicon. Additionally, the presence of intermetallic phases, particularly Mg_2Zn_{11}, and the microstructure redistribution through extrusion, leading to the week texture generation, played crucial roles in the strength increase. Despite achieving one of the highest tensile yield strengths (TYS) and UTS
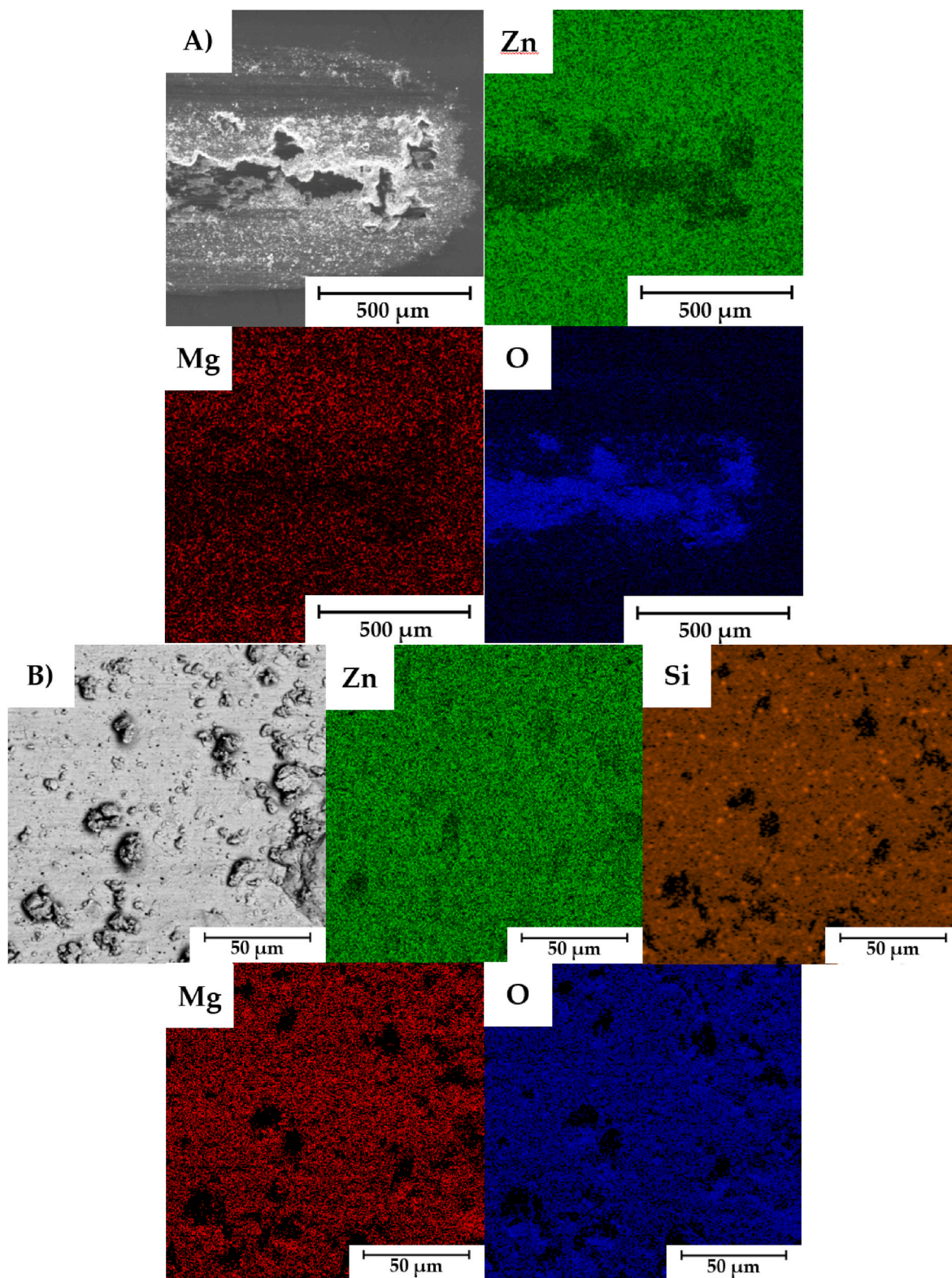
Fig. 16. Distribution of elements on the alloys after wear test (Scanning electron microscopy-Energy dispersive spectroscopy): A) Zn–1Mg^{SPS}, B) Zn–1Mg–1Si^{SPS + Ex}.

compared to other Zn–Mg alloys prepared by various techniques (Table 11), studied materials exhibited low plasticity. The oxide particles (generated during the extrusion of SPS materials and redistributed at grains boundaries) were primarily consisted of ZnO and MgO (Fig. 9). These hard and brittle particles or their localized aggregations could act as crack initiators within the soft surrounding matrix. Crack after

initiation could easily propagate through the material, resulting in reduced overall ductility.

Table 11 provides a concise comparison of the mechanical properties of selected Zn-based materials for biodegradable applications prepared by casting, extrusion, and rolling, alongside our prepared alloys. The Zn–1Mg casted alloy achieved inferior overall properties due to a
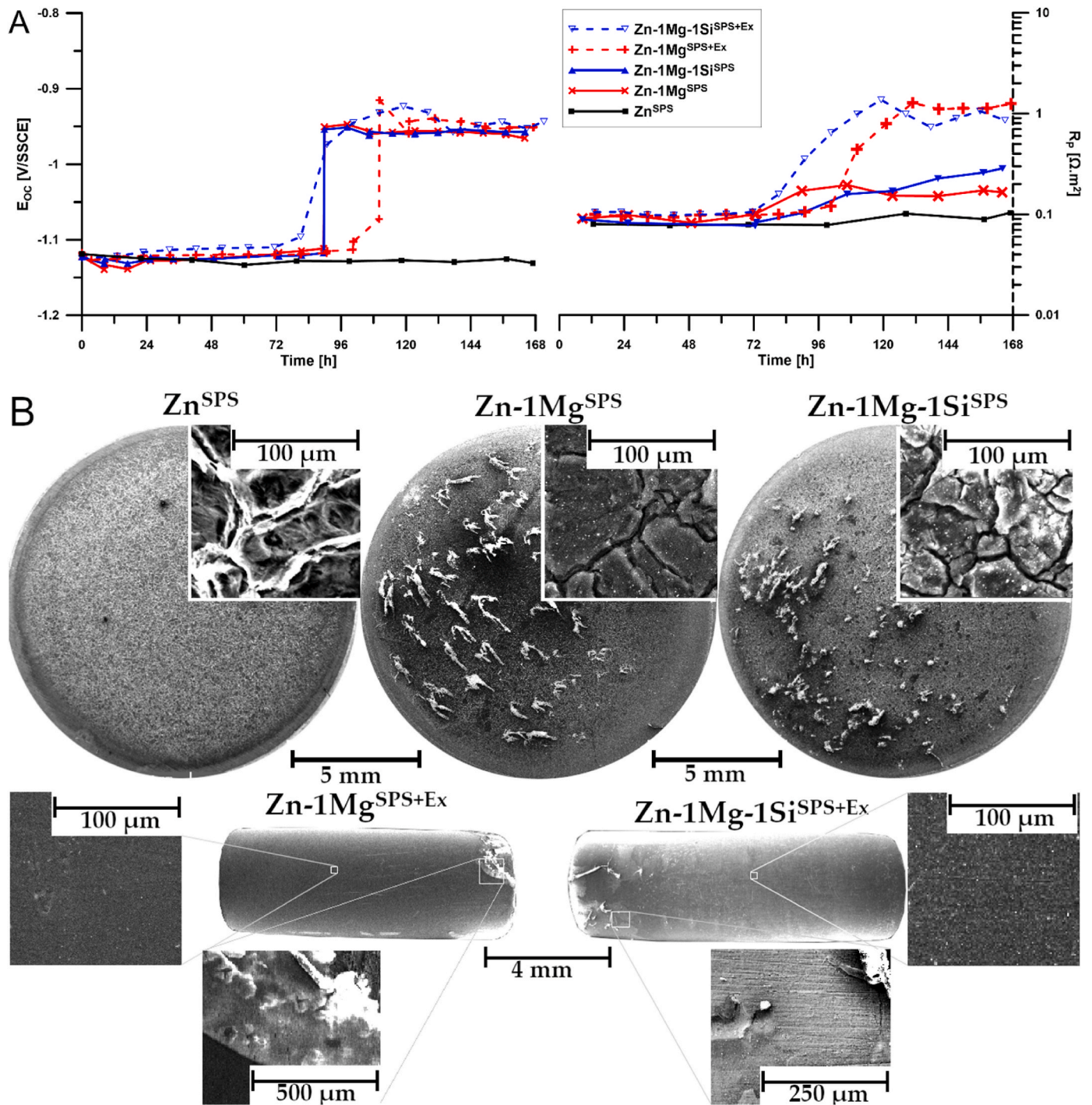
Fig. 17. The corrosion properties (Scanning electron microscopy): A) EOC and RP trends during 7-day exposure in L15 with 5% FBS; B) Surface of the samples after exposure.

coarser microstructure, composed of primary dendritic Zn grains and eutectic phases. Extrusion of the casted metal, as conducted by Gong et al. [56], significantly improved mechanical properties through strengthening mechanisms such as grain refinement and enhanced grain boundary strengthening. Nevertheless, the tensile strength (252 MPa) was notably lower than studied alloys prepared by SPS and extrusion. However, the lack of brittle oxide particles in the extruded material led to a higher elongation (13 %). Yang et al. [57] prepared Zn–Mg alloy by selective laser melting. Microstructure was consisted of eutectics, uniformly distributed along the grain boundaries. While it achieved higher results than pure zinc prepared by SLM due to various strengthening

mechanisms (grain strengthening, solid solution strengthening and precipitation strengthening), it did not surpass the results of the casted state.

The Zn–1Mg–1Si alloy was further compared to other ternary Zn–Mg based alloys, such as Zn–1Mg–1Ca [14], Zn–1Mg–xSr [14–16] and Zn–1Mg–xZr [58]. Casted metals alloyed with Sr and Ca achieved low mechanical properties, like binary Zn–1Mg alloy. The precipitation of intermetallic phases such as $MgZn_2$, $CaZn_{13}$ and $SrZn_{13}$ did not provide sufficient strengthening, and furthermore caused some brittleness. Therefore, Li et al. [14] used two types of thermomechanical processing in order to enhance alloy's properties: hot rolling and hot extrusion.

Table 10

Chemical composition of corrosion products after 7 days exposure in L-15 with 5 % FBS, %at. – SEM - EDS.

Sample	Site of analysis	C*	O*	Mg	Si	P	S	K	Cl	Ca	Zn
Zn^{SPS}	corroded surface	37.1	15.9	–	–	6.5	1.9	–	–	4.1	34.5
Zn–1Mg^{SPS}	corroded surface	20.1	22.9	1.7		9.2	0.6	–	–	6.2	39.3
	fibrous deposit	23.7	32.1	1.8		14.9	0.7	–	–	12.2	14.7
Zn–1Mg–1Si^{SPS}	corroded surface	22.4	25.1	1.6	6.2	10.7	0.7	–	–	7.9	25.4
	fibrous deposit	66.2	15.2	1.0	–	7.8		–	–	6.3	3.6
Zn–1Mg$^{SPS + Ex}$	corroded surface	27.4	24.3	1.9	–	12.7	1.5	0.4	0.6	8.1	22.9
	surroundings of fibers	34.7	25.3	0.9	–	7.1	0.8	0.2	3.6	3.8	23.6
Zn–1Mg–1Si$^{SPS + Ex}$	corroded surface	27.4	21.2	1.2	6.7	8.2	1.1	0.3	–	4.6	29.4
	surroundings of fibers	20.8	30.7	0.4	3.8	7.2	0.8	–	4.0	2.9	29.3

* light element analysis is only approximate, however, for the unexposed surface, both C and O are between 6.6 and 7.3 at. %

Table 11

Mechanical properties of selected zinc materials prepared by casting, hot rolling, extrusion, ECAP and selective laser melting.

Comp.	Preparation	Grain size [µm]	$\sigma_{TYS\,0,2}$ [MPa]	σ_{UTS} [MPa]	ε [%]	HV1	Reference
Zn	C	500	–	20	0.3	30	[23]
	HE	34	55 ± 8	97 ± 10	7.7 ± 2.7	44 ± 6	[59]
	HR	122	85	118	26.7	33	[60]
	SLM	104 ± 30	43 ± 3	61 ± 5	1.7 ± 0.1	50 ± 6	[57]
Zn–1Mg	C	–	94 ± 5	138 ± 5	0.5 ± 0.1	–	[56]
	HE	10	180 ± 4	252 ± 6	13 ± 2	–	
	SLM	10 ± 2.8	74 ± 4	126 ± 4	3.6 ± 0.2	93 ± 8	[57]
Zn–1Mg–1Ca	C	10–50	80 ± 9	131 ± 16	1.0 ± 0.3	92 ± 10	[14]
	HE	10–50	205 ± 10	257 ± 13	5.1 ± 1.0	–	
	HR	10–50	138 ± 9	198 ± 20	8.5 ± 1.3	107 ± 10	
Zn–1Mg–1Sr	C	–	87 ± 7	138 ± 9	1.3 ± 0.2	85 ± 2	
	HE	–	202 ± 5	253 ± 18	7.4 ± 1.3	–	
	HR	–	140 ± 10	201 ± 10	9.7 ± 1.0	92 ± 5	
Zn-0.8Mg-0.2Sr	HE	3.1	243 ± 2	315 ± 3	10.3 ± 0.3	–	[16]
	ECAP	2.5	200 ± 5	272 ± 5	12	–	[15]
Zn$^{SPS + Ex}$		–	74 ± 2	109 ± 5	18.3 ± 4	–	This work
Zn–1Mg$^{SPS + Ex}$	SPS + Ex	0.6 ± 0.3	227 ± 6	412 ± 4	2.0 ± 0.2	135 ± 3	
Zn–1Mg–1Si$^{SPS + Ex}$		0.4 ± 0.2	296 ± 24	422 ± 12	1.8 ± 0.6	137 ± 2	

C = casted, SLM = Selective Laser Melting, SPS = Spark Plasma Sintering, HE = Hot Extrusion, HR = hot rolling.

After hot rolling the grain sizes of prepared alloys became smaller and more homogeneous compared to their as-cast counterparts. This led to the increased ultimate compressive strength up to 201 MPa. Much better results were achieved by extrusion, which supports our intention to strengthen zinc materials using this process. Final mechanical properties achieved tensile yield strength of 205 ± 10 and 202 ± 5 and ultimate tensile strength of 257 ± 13 and 253 ± 18 for Zn–1Mg–1Ca and Zn–1Mg–1Sr alloys, respectively. Such values were still almost half of the strength achieved for the Zn–1Mg–1Si composite suggested in the presented paper.

Significant grain refinement was achieved for Zn-0.8Mg-0.2Sr prepared by extrusion or equal channel angular pressing (ECAP) but with the final grain size still above 1 µm. Works of Kubásek et al. [16] and Pinc et al. [15] shown significant effect of thermomechanical processing on microstructure, leading to the improvement of both strength and elongation. Alloy achieved UTS of 272 ± 5 MPa when prepared by ECAP and 315 ± 2 MPa when prepared by extrusion. This underscores the notable strengthening effect imparted by the extrusion method. However, it is important to note that, despite these achievements, these alloys did not attain the strength levels observed in presented materials.

4.3. Tribological properties

The tribological properties of zinc materials have been modestly described in the literature [61–63]. The friction coefficient indicates a relationship between normal and frictional force. Normal force is the force that surfaces exert to support objects and counteract the force of gravity, while frictional force is the force that opposes the motion or attempted motion of objects along surfaces due to interactions between surfaces. The value 0 means minimal friction between two materials. On the contrary, value 1 means that the frictional force is equal to the

normal force. When the friction coefficient is over 1, the frictional force is stronger than the normal one additional force is necessary to initiate motion (overcome the friction [64]).

The friction coefficient of prepared materials is higher compared to pure zinc, while the wear rate is perceptibly reduced. Such behavior is related to the presence of intermediate phases (Mg_2Zn_{11}, oxides), which increase the material hardness and therefore its wear resistance. Silicon addition in ternary alloys resulted in slightly faster loosening of the material during measurement. We believe that silicon particles are partially released from the zinc matrix and further support abrasive behavior at the interface of material and Al_2O_3 ball causing the increase of wear rate. Surprisingly the wear rate is increased for extruded materials compared to the materials prepared by SPS. This is related to the presence of oxide shells in the microstructure of SPS products. Oxide shells are deformed under the pressure of an Al_2O_3 ball and spread over the surface of the central part of the track (Figs. 15B and 16). The presence of Si partially disrupts this effect due to the interruption of the continuity of oxide shells in microstructure leading to the formation of individual islands of oxides on the surface instead of compact layer. Similarly, the extruded product does not contain a continuous network of oxide shells. Therefore, traces were covered by separated oxide fragmentations which may support abrasive behavior between the material and the Al_2O_3 ball instead of sliding of ball on large areas of deformed oxide shell. Unfortunately, it is difficult to compare tribological results from different tests due to the variations in setups generating incomparable results. Wang et al. [65] described the tribological and tribo-corrosion properties of Zn–Ti alloys prepared by casting or hot extrusion in Hanks solution on a high-speed reciprocating friction tester. The authors observed severe plastic deformation formed by abrasive wear with band-shaped debris formed by adhesive wear. Overall, the friction coefficient and wear loss decreased with the higher amount of

the alloying element (from 0.05 to 0.2 wt% of Ti) due to the precipitation of the hard $TiZn_{16}$ intermetallic phase. After hot extrusion, wider grooves were observed compared to the as-cast condition, indicating higher wear loss. Similar effects of processing on wear rate were reported by our results where SPS samples achieved better properties (lower friction coefficient and wear rate) compared to thermo-mechanically processed samples by extrusion.

In our research, we have observed a correlation between hardness and some tribological properties. Archard's law expresses the volume loss through equation (1), indicating that higher hardness corresponds to lower volume loss. Here, V represents the wear volume $[m^3]$, k is the constant referred to as the coefficient of wear (specific to the materials and conditions), F is the normal load [N] (set at 1 N in our research), s is the sliding distance in [m] (in our case 20 m) and HV is the hardness of the material (Table 9). Based on the obtained results, it is evident that as hardness increases, wear rate and footprint area decrease. However, considering equation (1) the value of "k" would be different for extruded and SPSed materials indicating differences in wear mechanism and comparability of materials according to the stated Archard's law. Comparable outcomes as in our case have been observed for Zn–Al alloy by Purcek et al. [66].

$$V = \frac{k \bullet s \bullet F}{HV} \qquad (1)$$

4.4. Corrosion properties

Corrosion tests in a complex body environment simulation verified the material's tendency towards relatively uniform degradation. A change in the corrosion reaction occurred during the exposure resulting in a significant slowing of dissolution. This was particularly the most evident for extruded materials (highest increase in the Rp). The extent of this slowing down is controlled by the presence of primary dissolution sites, such as the oxide shell region in non-extruded SPS-prepared materials. Alloying with magnesium leads to improved corrosion resistance and an increase in its concentration in the surface layer of the material, which is consistent with the proposed mechanism of limiting oxygen depolarization in the more complex layer of corrosion products [67,68]. The corrosion attack is primarily observed at the interface of zinc matrix and oxide shells containing a mixture of Zn and Mg. This leads to the dissolution of both Zn and Mg in the corrosion environment and the precipitation of corrosion products slightly enriched in Mg over the surface. Finally, the OCP is increased, and the corrosion rate decreases due to the change of the surface nature. Based on the analyses of chemical composition using EDS, corrosion products contained P, O, C, Cl, Zn, Mg and Ca, Si. The addition of silicon no longer significantly affects the dissolution rate, but the element appears on the surface at an even higher level than magnesium. In sum, carbonates, phosphates, chlorides, hydroxides, oxides, and their mixed compounds are expected on the material's surface after 1-week exposure (according to the literature [69–73]).

5. Conclusions

Zn–1Mg and Zn–1Mg–1Si materials were successfully prepared by powder metallurgy techniques including mechanical alloying, SPS, and extrusion. The obtained results indicated several key results:

1) The specific conditions of mechanical alloying including 800 RPM, 8 h of milling, ball to powder ratio equal to 10, and a ball diameter of 15 mm have been shown as optimized for the preparation of homogeneous powders with uniform distribution of Mg in the form of very fine intermediate particles (Mg_2Zn_{11}, MgO).
2) Silicon is presented in the Zn–1Mg–1Si in the form of homogeneously distributed particles.

3) The product compacted by both SPS and extrusion contained extremely fine grains with an average grain size below 0.5 μm.
4) Extruded Zn–1Mg–1Si is distinguished by superior tensile strength exceeding 400 MPa which is related to the combined strengthening effect of Mg_2Zn_{11}, Zn(Mg)O, and Si.
5) Both Zn–1Mg and Zn–1Mg–1Si reached lower wear rates compared to the pure zinc, although additional extrusion caused the increased wear rate of the materials compacted by SPS.
6) The corrosion rate of Zn–1Mg, Zn1Mg–1Si is slightly decreased after initial corrosion onset as a consequence of the formation of corrosion products enriched in Mg, C, P, O, Ca, and Si.
7) Studied materials could be used for a variety of low-load-bearing orthopedic applications that are stressed primarily in compression. Due to their similarity to bio-ceramics, applications like augmentation, fillings inside the human bone or screws are suggested.

Data availability statement

The data used in this article is located in the Zenodo repository under link https://doi.org/10.5281/zenodo.10371468.

Declaration of competing interest

The authors declare that they have no known competing financial interests or personal relationships that could have appeared to influence the work reported in this paper.

References

[1] Hench LL, Thompson I. Twenty-first century challenges for biomaterials. J R Soc Interface 2010;7(suppl_4):S379–91.
[2] Kabir H, et al. Recent research and progress of biodegradable zinc alloys and composites for biomedical applications: biomechanical and biocorrosion perspectives. Bioact Mater 2021;6(3):836–79.
[3] Redlich C, et al. In vitro degradation behavior and biocompatibility of bioresorbable molybdenum. Metals 2021;11(5).
[4] Li H, Zheng Y, Qin L. Progress of biodegradable metals. Prog Nat Sci: Mater Int 2014;24(5):414–22.
[5] Seitz J-M, et al. Recent advances in biodegradable metals for medical sutures: a critical review. Adv Healthcare Mater 2015;4(13):1915–36.
[6] Pospíšilová I, Vojtěch D. Zinc alloys for biodegradable medical implants. Mater Sci Forum 2014;782:457–60.
[7] Kubásek J, et al. Microstructure and mechanical properties of the micrograined hypoeutectic Zn–Mg alloy. Int J Miner Metall Mater 2016;23(10):1167–76.
[8] Lou D, et al. Textural evolution and improved ductility in Zn-0.2Mg-0.8Mn (wt%) alloys at different extrusion temperatures. J Alloys Compd 2021;860:158530.
[9] Tang Z, et al. Design and characterizations of novel biodegradable Zn-Cu-Mg alloys for potential biodegradable implants. Mater Des 2017;117:84–94.
[10] Niu J, et al. Research on a Zn-Cu alloy as a biodegradable material for potential vascular stents application. Mater Sci Eng C 2016;69:407–13.
[11] Zhu S, et al. Microstructure, mechanical properties and creep behaviour of extruded Zn-xLi (x = 0.1, 0.3 and 0.4) alloys for biodegradable vascular stent applications. Mater Sci Eng, A 2020;777:139082.
[12] Zhao S, et al. Zn-Li alloy after extrusion and drawing: structural, mechanical characterization, and biodegradation in abdominal aorta of rat. Mater Sci Eng C 2017;76:301–12.
[13] Yang X, et al. Optimization of mechanical properties and corrosion resistance of Zn-0.4Mn-0.8Li alloy using the hot rolling process. J Mater Sci Technol 2023;145:136–47.
[14] Li H, et al. Design and characterizations of novel biodegradable ternary Zn-based alloys with IIA nutrient alloying elements Mg, Ca and Sr. Mater Des 2015;83:95–102.

[15] Pinc J, et al. Microstructure evolution and mechanical performance of ternary Zn-0.8Mg-0.2Sr (wt. %) alloy processed by equal-channel angular pressing. Mater Sci Eng, A 2021;824.

[16] Kubásek J, et al. The evolution of microstructure and mechanical properties of Zn-0.8Mg-0.2Sr alloy prepared by casting and extrusion. J Alloys Compd 2022;906: 164308.

[17] Čapek J, et al. Extrusion of the biodegradable ZnMg0.8Ca0.2 alloy – the influence of extrusion parameters on microstructure and mechanical characteristics. J Mech Behav Biomed Mater 2020;108:103796.

[18] Hernández-Escobar D, et al. Current status and perspectives of zinc-based absorbable alloys for biomedical applications. Acta Biomater 2019;97:1–22.

[19] Vojtech D, et al. Mechanical and corrosion properties of newly developed biodegradable Zn-based alloys for bone fixation. Acta Biomater 2011;7(9): 3515–22.

[20] Mostaed E, et al. Zinc-based alloys for degradable vascular stent applications. Acta Biomater 2018;71:1–23.

[21] Jarzębska A, et al. A new approach to plastic deformation of biodegradable zinc alloy with magnesium and its effect on microstructure and mechanical properties. Mater Lett 2018;211:58–61.

[22] Jarzębska A, et al. Controlled grain refinement of biodegradable Zn-Mg alloy: the effect of magnesium alloying and multi-pass hydrostatic extrusion preceded by hot extrusion. Metall Mater Trans 2020;51(12):6784–96.

[23] Kubasek J, Vojtěch D. Zn-based alloys as an alternative biodegradable materials. Proc. Metal 2012;5:23–5.

[24] Zhou W, et al. Effect of micropore/microsphere topography and a silicon-incorporating modified titanium plate surface on the adhesion and osteogenic differentiation of BMSCs. Artif Cell Nanomed Biotechnol 2020;48(1):230–41.

[25] Jiao Y, et al. Microstructure and biological activity of silicon-doped composite coatings fabricated by micro-arc oxidation on magnesium alloy. Surf Interface Anal 2021;53(2):277–84.

[26] De Negri S, et al. The Mg–Zn–Si system: constitutional properties and phase formation during mechanical alloying. Intermetallics 2010;18(9):1722–8.

[27] Gao C, et al. Nano-SiC reinforced Zn biocomposites prepared via laser melting: microstructure, mechanical properties and biodegradability. J Mater Sci Technol 2019;35(11):2608–17.

[28] Mei Z, et al. Microstructure investigation of a SiC whisker reinforced eutectoid zinc alloy matrix composite. Compos Appl Sci Manuf 2006;37(9):1345–50.

[29] Nagaral M, et al. Characterization and tensile fractography of nano ZrO2 reinforced copper-zinc alloy composites. Frat Ed Integrità Strutt 2019;13(48):370–6.

[30] Li K, et al. New biodegradable Mg–Zn–Ca bulk metallic glass composite with large plasticity reinforced by SnZn alloy. Mater Sci Eng, A 2023;873:145045.

[31] Li K, et al. Core-shell Mg66Zn30Ca4 bulk metallic glasses composites reinforced by Fe with high strength and controllable degradation. Intermetallics 2021;138: 107334.

[32] Li K, et al. Mechanical properties and corrosion resistance of powder metallurgical Mg-Zn-Ca/Fe bulk metal glass composites for biomedical application. J Mater Sci Technol 2022;103:73–83.

[33] Liu X, et al. Effects of alloying elements (Ca and Sr) on microstructure, mechanical property and in vitro corrosion behavior of biodegradable Zn–1.5Mg alloy. J Alloys Compd 2016;664:444–52.

[34] Miranda-Hernández JG, et al. Synthesis and characterization of Zn-Ni advanced alloys prepared by mechanical milling and sintering at solid-state process. Adv Mater Sci Eng 2017;2017:7967848.

[35] Suryanarayana C, Ivanov E, Boldyrev VV. The science and technology of mechanical alloying. Mater Sci Eng, A 2001;304–306:151–8.

[36] Xie D, Takada H, Kanetaka H. Development of high performance MgFe alloy as potential biodegradable materials. Mater Sci Eng, A 2016;671:48–53.

[37] Necas D, et al. Advanced zinc-magnesium alloys prepared by mechanical alloying and spark plasma sintering. Materials 2022;15(15).

[38] Nečas D, et al. Ultrafine-grained Zn-Mg-Sr alloy synthesized by mechanical alloying and spark plasma sintering. Materials 2022;15. https://doi.org/10.3390/ ma15238379.

[39] Pinc J, et al. Microstructural characterization and optimization of the ZnMg0.8 (CaO)0.26 alloy processed by ball milling and subsequent extrusion. Manufacturing Technol 2020;20:484–91.

[40] Guezmil M, et al. Effect of test parameters on the friction behaviour of anodized aluminium alloy. Int Sch Res Notices 2014:1–9. 2014.

[41] Hybasek V, et al. Influence of model environment complexity on corrosion mechanism of biodegradable zinc alloys. Corrosion Sci 2021;187:109520.

[42] Klíma K, et al. Zn–0.8Mg–0.2Sr (wt.%) absorbable screws—an in-vivo biocompatibility and degradation pilot study on a rabbit model. Materials 2021;14 (12):3271.

[43] Lesz S, et al. Characterisation of Mg-Zn-Ca-Y powders manufactured by mechanical milling. J Achievements in Mater Manufacturing Eng 2020;2:49–59.

[44] Li K, et al. Effect of powder size on strength and corrosion behavior of Mg66Zn30Ca4 bulk metallic glass. J Alloys Compd 2022;897:163219.

[45] Krystýnová M, et al. Preparation and characterization of zinc materials prepared by powder metallurgy. Metals 2017;7(10).

[46] Suryanarayana C. Mechanical alloying and milling. Prog Mater Sci 2001;46(1): 1–184.

[47] Salleh EM, Ramakrishnan S, Hussain Z. Synthesis of biodegradable Mg-Zn alloy by mechanical alloying: effect of milling time. Procedia Chem 2016;19:525–30.

[48] Dambatta MS, et al. Processing of Zn-3Mg alloy by equal channel angular pressing for biodegradable metal implants. J King Saud Univ Sci 2017;29(4):455–61.

[49] Hernández-Escobar D, et al. Microstructural evolution and intermetallic formation in Zn-Mg hybrids processed by High-Pressure Torsion. Phil Mag 2019;99(5): 557–84.

[50] Yang H, et al. In vitro and in vivo studies on zinc-hydroxyapatite composites as novel biodegradable metal matrix composite for orthopedic applications. Acta Biomater 2018;71:200–14.

[51] Čapek J, et al. Microstructural, mechanical, in vitro corrosion and biological characterization of an extruded Zn-0.8Mg-0.2Sr (wt%) as an absorbable material. Mater Sci Eng C 2021;122:111924.

[52] Shen C, et al. Mechanical properties, in vitro degradation behavior, hemocompatibility and cytotoxicity evaluation of Zn–1.2Mg alloy for biodegradable implants. RSC Adv 2016;6(89):86410–9.

[53] Wang Y, Huang J. Texture analysis in hexagonal materials. Mater Chem Phys 2003; 81(1):11–26.

[54] Lassila D, LeBlanc M, Florando J. Zinc single-crystal deformation experiments using a "6 degrees of freedom" apparatus. Metall Mater Trans 2007;38:2024–32.

[55] Mayama T, et al. Crystal plasticity analysis of texture development in magnesium alloy during extrusion. Int J Plast 2011;27(12):1916–35.

[56] Gong H, et al. In vitro biodegradation behavior, mechanical properties, and cytotoxicity of biodegradable Zn–Mg alloy. J Biomed Mater Res B Appl Biomater 2015;103(8):1632–40.

[57] Yang Y, et al. A combined strategy to enhance the properties of Zn by laser rapid solidification and laser alloying. J Mech Behav Biomed Mater 2018;82:51–60.

[58] Ren T, et al. Evaluation of as-extruded ternary Zn–Mg–Zr alloys for biomedical implantation material: in vitro and in vivo behavior. Mater Corros 2019;70(6): 1056–70.

[59] Sikora-Jasinska M, et al. Fabrication, mechanical properties and in vitro degradation behavior of newly developed ZnAg alloys for degradable implant applications. Mater Sci Eng C 2017;77:1170–81.

[60] Liu S, et al. Effects of deformation twinning on the mechanical properties of biodegradable Zn-Mg alloys. Bioact Mater 2019;4:8–16.

[61] Li H, et al. Investigation on tribological behaviors of biodegradable pure Zn and Zn-X (Li, Cu, Ge) binary alloys. J Mater Sci Mater Med 2021;32(12):149.

[62] Babic M, Mitrovic S, Ninković R. Tribological potential of zinc-Aluminium alloys improvement. Tribol Ind 2009;31:15–28.

[63] Lo SHJ, et al. Mechanical and tribological properties of zinc-aluminium metal-matrix composites. J Mater Sci 1992;27(21):5681–91.

[64] Lenard JG. 9 - tribology. In: Lenard JG, editor. Primer on flat rolling. second ed. Oxford: Elsevier; 2014. p. 193–266.

[65] Wang K, et al. Binary Zn–Ti alloys for orthopedic applications: corrosion and degradation behaviors, friction and wear performance, and cytotoxicity. J Mater Sci Technol 2021;74:216–29.

[66] Purcek G, et al. Dry sliding friction and wear properties of zinc-based alloys. Wear 2002;252:894–901.

[67] Stoulil J, et al. Electrochemical properties of corrosion products formed on Zn-Mg, Zn-Al and Zn-Al-Mg coatings in model atmospheric conditions. Mater Corros 2015; 66(8):777–82.

[68] Prosek T, et al. Corrosion mechanism of model zinc–magnesium alloys in atmospheric conditions. Corrosion Sci 2008;50(8):2216–31.

[69] Pinc J, et al. A detailed mechanism of degradation behaviour of biodegradable as-ECAPed Zn-0.8Mg-0.2Sr with emphasis on localized corrosion attack. Bioact Mater 2023;27:447–60.

[70] Jiang W, Yu W. Corrosion behavior and osteogenic activity of a biodegradable orthopedic implant Mg–Si alloy with a gradient structure. Metals 2021;11. https:// doi.org/10.3390/met11050781.

[71] Beaussant Törne K, Örnberg A, Weissenrieder J. Characterization of the protective layer formed on zinc in whole blood. Electrochim Acta 2017;258:1476–83.

[72] Alves MM, et al. Evolution of the in vitro degradation of Zn–Mg alloys under simulated physiological conditions. RSC Adv 2017;7(45):28224–33.

[73] Almathami S, et al. Exploring the influence of biologically relevant ions on the corrosion behavior of biodegradable zinc in physiological fluids. ACS Biomater Sci Eng 2023;9(5):2301–16.